Classification of slip system interaction in microwires under torsion

Kolja Zoller[a,c], Patric Gruber[a], Michael Ziemann[a], Alexander Görtz[a], Peter Gumbsch[a,b], Katrin Schulz[a,c,*]

[a]*Karlsruhe Institute of Technology (KIT), Institute for Applied Materials (IAM), Karlsruhe, Germany*
[b]*Fraunhofer Institute for Mechanics of Materials IWM, Freiburg, Germany*
[c]*Karlsruhe University of Applied Sciences, Karlsruhe, Germany*

Abstract

Microwires have become of increasing interest for the miniaturization of structural components. A profound understanding of the deformation behavior of microwires is important for the the assessment of their applicability and lifetime in specific components. In particular, the deformation behavior under torsional loading and the associated microstructure evolution are of interest. The exact involvement of individual slip systems and their activities in the complex stress field under torsional loading are mostly unknown. In this paper, the microstructure evolution of single crystalline gold microwires under torsion have been analyzed for the high-symmetry crystal orientations $\langle 1\,0\,0 \rangle$, $\langle 1\,1\,0 \rangle$, and $\langle 1\,1\,1 \rangle$ using simulation and experimental results. It is shown that a classification of the slip systems can be derived a priori by theoretical considerations. It is found, that the slip system activity, stress relaxation mechanism, as well as screw and edge composition of the piled-up dislocation density depends on specific slip system groups. Furthermore, the misorientation and its rotational axes including the identification of the slip system activities are discussed.

1. Introduction

The importance of a profound understanding of the underlying microstructure evolution of metals is emphasized by size effects observed for systems at the microscale. This is of increasing interest due to the miniaturization of structural components and particularly pronounced for torsional loads [2, 3, 4]. The torsional loading leads to complex stress fields, microstructure evolution, and dislocation structures involving internal pile-ups of geometrically necessary dislocations (GNDs) as well as interaction of different slip systems, e.g. [5, 6, 7, 8].

Based on the inhomogeneous stress field, the Schmid factor variation of the individual slip systems along the circumference induce locally varying slip system activities [9]. The orientation dependency of the formed dislocation structures were studied using molecular dynamics (MD) simulations of single crystalline gold and aluminium nanowires under torsion with high symmetry orientations in [5, 10] as well as in discrete dislocation dynamics (DDD) simulations of single crystalline copper nanowires [8]. It has been observed that dislocations align parallel to the torsion axis in the $\langle 1\,1\,0 \rangle$ orientation, whereas the dislocation lines are oriented orthogonal to the torsion axis in the $\langle 1\,0\,0 \rangle$ and $\langle 1\,1\,1 \rangle$ orientations and form dislocation networks that lead to twist boundaries. Dislocations can cross the neutral axis of the corresponding slip systems due to the dislocation interaction in the internal pile-ups, as observed in DDD-simulations of single crystalline aluminium and experiments on bamboo-structured gold microwires with $\langle 1\,0\,0 \rangle$ and $\langle 1\,1\,1 \rangle$ orientations [11]. The observed Bauschinger effect for microwires subjected to cyclic torsion loading can be explained

by the back stress. The back stress introduces reverse motion of dislocations from the pile-ups during unloading [6, 12]. The dislocation network densifies with increasing plastic deformation, permanently stabilizing the dislocation structure, as shown by DDD-simulations of single crystalline aluminium nanowires with $\langle 1\,0\,0 \rangle$ and $\langle 2\,3\,4 \rangle$ orientations subjected to cyclic torsion loading [6]. In the $\langle 1\,0\,0 \rangle$ orientation, dislocations are active on all slip planes and the superposition of the resulting individual twist components leads to a global twist around the torsion axis [11]. The coaxial and hexagonal network structures in the $\langle 1\,1\,0 \rangle$ and $\langle 1\,1\,1 \rangle$ orientations exhibit significant plastic recovery during unloading, whereas the rectangular network structures in the $\langle 1\,0\,0 \rangle$ orientation are more stable and lead to less plastic recovery [13].

While MD and DDD simulations are limited to system sizes ranging from the nanoscale to a few micrometers due to numerical costs, continuum formulations yield access to larger volumes. Using continuum approaches, some approaches localize the accumulation of the GND density, neglecting the network formation during dislocation motion, only in the inner, near-center region of the wire [14, 15]. The experimentally and simulatively observed size effects at the onset of yielding for microwires under torsion can be attributed to geometrical restrictions [16]. This coincides with the critical thickness effect [17]. Furthermore, the accumulation and pile-up of GNDs within the system lead to a size effect in the material hardening [16, 18]. Thereby, the texture of the individual grains influences the size effect due to the different slip system orientations in the respective grains based on oligocrystalline gold microwires with $\langle 1\,0\,0 \rangle$ and $\langle 1\,1\,1 \rangle$ orientations as shown in [19]. The overall deformation structures are related to the activated slip systems in the grains as shown by the experimental investigation of the misorientation resulting from the microstructure evolution

---

*Corresponding author.
 Email address: katrin.schulz@kit.edu (Katrin Schulz)

in bamboo-structured gold microwires with $\langle 1\,0\,0 \rangle$ and $\langle 1\,1\,1 \rangle$ orientations in [20]. Approaches to determine the GND density on the individual slip systems from the dislocation density tensors derived by experimental investigations are pursued in [21, 22].

One big remaining challenge is to analyze the dislocation density with respect to the different dislocation types, such as e.g. edge or screw type with their corresponding orientation. This information about the composition of the dislocation density on the individual slip systems is important to understand network evolution and to permit a realistic modelling of the latter on a continuum scale. Modern Continuum Dislocation Dynamics (CDD) simulations [23, 24, 25, 26, 27] are in principle capable of incorporating the elementary dislocation reaction mechanisms during the dislocation network evolution, like cross slip of screw dislocations or other dislocation reactions. However, experimental information on the character of individual dislocations is very difficult to determine on a larger scale. The exact involvement, interaction and impact of the individual slip systems is largely unknown and surface analyses on scanning electron microscopy images can, e.g., only identify the involved slip planes but not the slip systems.

In this work, we present an analysis and classification of the slip system activities for single crystalline fcc microwires under torsional loading. We combine theoretical analyses, CDD simulations and experiments to provide comprehensive and direct insight into the microstructure evolution. We investigate the composition of the dislocation densities and the interaction of the slip system activities with respect to the resulting misorientation. Based on the misorientation, a new approach to identify the activities of individual slip system groups is proposed.

2. Methods and Materials

In this work, theoretical considerations as well as simulations and experiments are used to gain insight into the microstructure

evolution of single crystalline fcc (Au) microwires under torsion.

2.1. System Analysis

To get insights into the slip system activities, their interactions, as well as their impact on the misorientation, a detailed system analysis based on theoretical considerations is done a priori. We focus on the three high-symmetry crystal orientations $\langle 1\,0\,0 \rangle$, $\langle 1\,1\,0 \rangle$, and $\langle 1\,1\,1 \rangle$.

Geometrical aspects

The torsional loading leads to shear stresses in the circumferential direction in the wire cross-section. In the purely elastic case, the shear stresses increase linearly from the center axis to the circumference surface. It holds

$$\sigma^{\text{ext}}(r, \phi) = \tau^{\text{ext}}(r)(\boldsymbol{e}_\phi \otimes \boldsymbol{e}_y + \boldsymbol{e}_y \otimes \boldsymbol{e}_\phi), \qquad \boldsymbol{e}_\phi = \cos\phi\,\boldsymbol{e}_x - \sin\phi\,\boldsymbol{e}_z.$$
(1)

Here, $\{r, \phi, y\}$ describes the cylinder coordinate system and $\{x, y, z\}$ the Cartesian coordinate system used, see Figure 1. Thus, the external stress field σ^{ext} is inhomogeneous and dislocation pile-ups are expected inside the system, whereby the orientation of the pile-ups depends on the individual slip system. To assess the slip system activities depending on the crystal orientation, the Schmid factor m_s is used. The Schmid factor projects the stress state onto the respective slip system s by means of the Schmid tensor $\boldsymbol{M}_s$, which is characterized by the slip direction $\boldsymbol{d}_s$ and slip plane normal $\boldsymbol{m}_s$:

$$m_s = \boldsymbol{M}_s \cdot {}^{1}\!/_{\tau^{\text{ext}}}\, \sigma^{\text{ext}}(x, z), \qquad M_s = \boldsymbol{d}_s \otimes \boldsymbol{m}_s.$$
(2)

Due to the inhomogeneous stress field, the Schmid factors of the slip systems vary locally. For a classification of the slip systems, the maximum Schmid factors m_s^{max} occurring on the
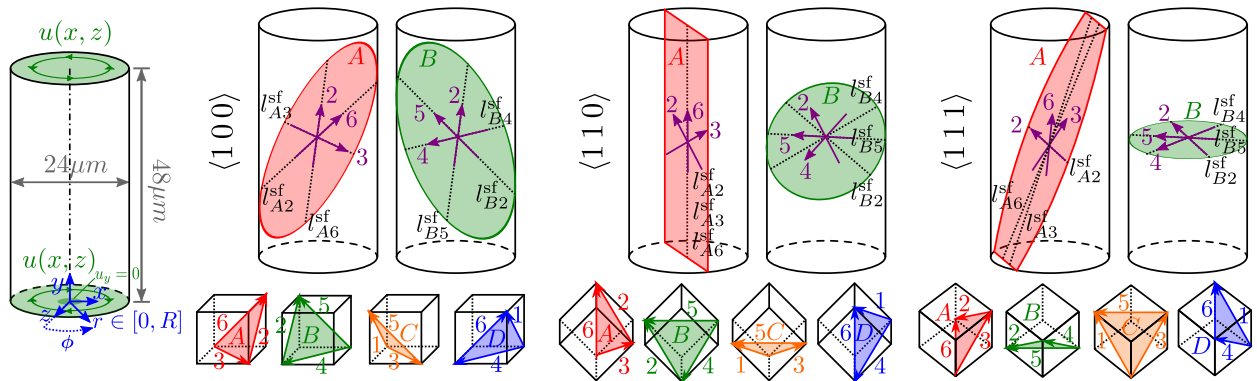
Figure 1: System configuration of the considered microwires under torsion as well as the spatial orientation of the individual slip systems and the respective stress-free lines l_s^{sf} in the microwires under torsion in dependence on the crystal orientation. The slip systems are labeled according to the Schmid-Boas notation [1] with letters (A, B, C, D) for the slip planes and numbers for the slip directions. For a $\langle 1\,0\,0 \rangle$ crystal orientation, the slip planes C and D behave analogously to A and B. For the $\langle 1\,1\,0 \rangle$ crystal orientation, the slip planes C behave analogously to B and slip plane D analogously to A, whereas for a $\langle 1\,1\,1 \rangle$ crystal orientation, the slip planes C and D behave analogously to A.

2

		A2	A3	A6	B2	B4	B5	C1	C3	C5	D1	D4	D6
$\langle 1\,0\,0\rangle$:	m_s^{max}	0.4	0.6	0.4	0.4	0.6	0.4	0.4	0.6	0.4	0.4	0.6	0.4
	ϕ_s^{max}	0°	−45°	90°	0°	45°	90°	0°	−45°	90°	0°	45°	90°
	Screw	25%	100%	25%	25%	100%	25%	25%	100%	25%	25%	100%	25%
	Edge	75%	0%	75%	75%	0%	75%	75%	0%	75%	75%	0%	75%
$\langle 1\,1\,0\rangle$:	m_s^{max}	0.5	0.5	1	0.5	0.5	0.8	0.5	0.5	0.8	0.5	0.5	1
	ϕ_s^{max}	35°	35°	35°	−35°	35°	0°	35°	−35°	0°	−35°	−35°	−35°
	Screw	25%	25%	100%	89%	89%	100%	89%	89%	100%	25%	25%	100%
	Edge	75%	75%	0%	11%	11%	0%	11%	11%	0%	75%	75%	0%
$\langle 1\,1\,1\rangle$:	m_s^{max}	0.3	0.7	0.7	1	1	1	0.7	0.7	0.3	0.7	0.3	0.7
	ϕ_s^{max}	−60°	44°	16°	−60°	60°	0°	−76°	76°	0°	−44°	60°	−16°
	Screw	100%	68%	68%	100%	100%	100%	68%	68%	100%	68%	100%	68%
	Edge	0%	32%	32%	0%	0%	0%	32%	32%	0%	32%	0%	32%

Table 1: Maximum Schmid factors and corresponding angles of the individual slip systems depending on the crystal orientation for microwires under torsion, as well as the screw and edge parts of fictitious GNDs parallel to the respective stress-free lines.

individual slip systems are used and are calculated by

$$m_s^{\mathrm{max}} = \max_\phi(|\boldsymbol{M}_s \cdot \frac{1}{\tau^{\mathrm{ext}}} \, \sigma^{\mathrm{ext}}(\phi)|) = \qquad (3)$$
$$|\boldsymbol{M}_s \cdot (\cos \phi_s^{\mathrm{max}}(\boldsymbol{e}_x \otimes \boldsymbol{e}_y + \boldsymbol{e}_y \otimes \boldsymbol{e}_x) - \sin \phi_s^{\mathrm{max}}(\boldsymbol{e}_y \otimes \boldsymbol{e}_z + \boldsymbol{e}_z \otimes \boldsymbol{e}_y))|.$$

Here, ϕ_s^{max} describes the angle at which the respective Schmid factor becomes maximal. The resulting values of m_s^{max} and ϕ_s^{max} are listed in Table 1.

The projection of the stress-free line $\boldsymbol{l}_s^{sf}$ of the respective slip system onto the cross-section of the wire (plane normal in y-direction) can be specified via the corresponding unit vector $\boldsymbol{e}_{\phi^{\mathrm{max}}} = (\cos \phi_s^{max}, 0, -\sin \phi_s^{max})^T$ and passes the torsion axis. The specification of the direction vector $\boldsymbol{e}_{\boldsymbol{l}_s^{sf}}$ of the stress-free line on the respective slip plane is done by calculating the y-component via the restriction $\boldsymbol{e}_{\boldsymbol{l}_s^{sf}} \cdot \boldsymbol{m}_s = 0$ and a subsequent normalization: $\|\boldsymbol{e}_{\boldsymbol{l}_s^{sf}}\| = 1$. The spatial orientations of the individual slip systems and the respective stress-free lines in the microwires under torsional loading are illustrated in Figure 1. Considering the orientation of the respective Burgers vectors, the screw part of a fictional GND parallel to the stress-free line on the individual slip planes can be calculated by $(\boldsymbol{e}_{\boldsymbol{l}_s^{sf}} \cdot \boldsymbol{d}_s)^2$ and are listed in Table 1.

Based on the maximum Schmid factors, a classification of the slip systems can be proposed depending on the crystal orientation. Additionally, the dislocation reactions between the slip systems are also takes into account. This is reasonable for the $\langle 1\,1\,0\rangle$ orientation, since, e.g., glissile reactions involving the primary (highest Schmid factors) slip system group {A6,D6} only form new dislocation segments on the slip systems {A2,A3,D1,D4}, but not on the slip systems {B2,B4,C1,C3}. Consequently, these two groups are expected to behave differently during the microstructure evolution, although they share the same maximum Schmid factor. The resulting slip system classification is given in Table 2.

	$\tilde{S}$	Highest m_s^{max}	Further slip system groups
$\langle 1\,0\,0\rangle$	2	{B4,C3,A3,D4}	{B2,B5,C1,C5,A2,A6,D1,D6}
$\langle 1\,1\,0\rangle$	4	{A6,D6}	{B5,C5}, {A2,A3,D1,D4}, {B2,B4,C1,C3}
$\langle 1\,1\,1\rangle$	3	{B2,B4,B5}	{C1,C3,A3,A6,D1,D6}, {C5,A2,D4}

Table 2: Slip system groups based on the Schmid factors and dislocation reactions depending on the crystal orientation. Here $\tilde{S}$ describe the number of slip system groups.

Interaction of slip system activities

In the following, the stress relaxation mechanism of the slip system groups will be analyzed. Considering small deformations, the elastic strain $\varepsilon^{\mathrm{el}}$ describes the symmetric, elastic part of the distortion tensor $\mathbf{Du}$. The distortion tensor can be additively decomposed into the elastic part $\boldsymbol{\beta}^{\mathrm{el}}$ and the plastic part $\boldsymbol{\beta}^{\mathrm{pl}}$. The plastic distortion results solely from the plastic slip γ_s on the individual slip systems given by

$$\boldsymbol{\varepsilon}^{\mathrm{el}} = \mathrm{sym}(\boldsymbol{\beta}^{\mathrm{el}}), \qquad \boldsymbol{\beta}^{\mathrm{el}} = \mathbf{Du} - \boldsymbol{\beta}^{\mathrm{pl}}, \qquad \boldsymbol{\beta}^{\mathrm{pl}} = \sum_{s=1}^{S} \gamma_s \mathbf{M}_s. \quad (4)$$

Consequently, there are two different mechanisms of stress relaxation which are visualized in Figure 2 (Step: *Loaded → Relaxed*) for a simplified system under shear loading:

(I) *Transformation*, see (a)→(b): The plastic slip takes place on a plane parallel to the shear loading plane and transforming the elastic into plastic deformation.

(II) *Counterpart*, see (a)→(c): The plastic slip takes place on a plane perpendicular to the shear loading plane creating an elastic counterpart to the elastic shear loading. The two transposed elastic components cancel each other out
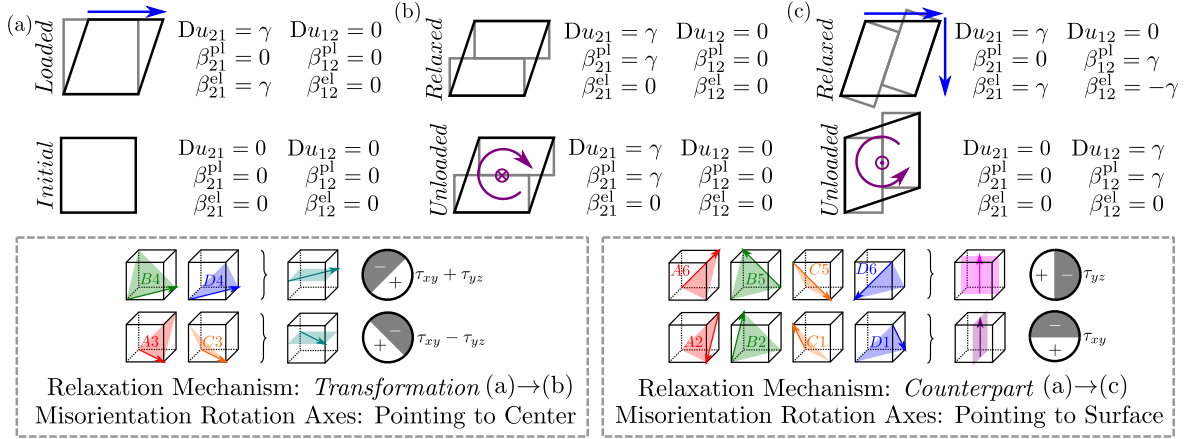
Figure 2: Visualization of the two stress relaxation mechanisms ((a)→(b) and (a)→(c)), whereby the deformed structure is shown in black, the elastic deformation is represented by blue arrows, the plastic deformation is drawn in gray, and the rotation due to the plastic deformation is represented by purple arrows. Additional, the combination of different slip system activities to the plastic deformation due to one representative slip system and the relevant external stress components for the dislocation velocity are shown for a $\langle 1\,0\,0\rangle$ crystal orientation and torsional loading.

in the stress calculation (see sym operator in Equation 4) and lead to a rotation due to the skew-symmetric character.

After unloading, the different orientations of the plastic deformation are visible and lead to an opposite direction of the rotation axis of the misorientation between the two deformation states (b) and (c) (compare the calculation rule of the misorientation in section Appendix A in the appendix). In the considered, simplified loading case, the rotation axis for the relaxation mechanism 'Transformation' points into the drawing plane (whose normal is orthogonal to the normal of the slip plane and loading plane as well as to the slip direction). In contrast, the rotation axis for the relaxation mechanism 'Counterpart' points out of the drawing plane. The direction of the rotation axes depends on the load direction. Transferred to the torsional load, the rotation axes of the misorientation point to the center of the cross-section for the relaxation mechanism Transformation, whereas they points outward to the surface for the relaxation mechanism Counterpart. This leads to the hypothesis that the direction of the roatation axes of misorientation provides information about slip system activities. Therefore, the relaxation mechanisms of the individual slip system groups are identified based on the resulting plastic distortion due to the slip systems activities according to Equation 4. The slip system activities can be combined to the activity of one representative slip system respectively, as shown in Figure 2 for the $\langle 1\,0\,0\rangle$ crystal orientation.

2.2. Dislocation density based continuum model

Using a higher dimensional space, a kinematically closed CDD formulation can be derived, that preserves information about the orientations of the dislocations and allows the description of the motion of homogenized curved dislocations in 3d [23, 24, 28]. In this paper, a CDD formulation based on the formulation introduced in [25] is used. In accordance to [27],

we divide the total dislocation density into a mobile dislocation density, yielding plastic deformation, and a dislocation network density, contributing to the material hardening. We consider both dislocation motion hindrance due to Lomer and collinear reactions and dislocation multiplication due to glissile reactions and cross-slip following the model in [26]. This is complemented by a homogenized dislocation source model introduced in [29]. The constitutive law for the dislocation velocity considers internal stresses including eigenstresses of the dislocations according to [30] and short-range dislocation stress interaction covered by a back stress term in accordance to [31, 32]. A yield stress term based on [33] is used to model the hardening due to the interaction with forest dislocations from other slip systems within the averaging volume. The stress-strain relation describes physical linearity using the cubic symmetry of the elasticity tensor. A visualization of the degrees of freedom of the CDD formulation used can be found in [34].

In the following, the parameters used in the simulations and the corresponding references are listed. In the calculation of the Cauchy stress field resulting from the external loading by means of the three-dimensional Hooke's law, the anisotropic elastic constants of gold were set to $\{C_{1111} = 186\,\text{GPa}, C_{1122} = 157\,\text{GPa}, C_{2323} = 42\,\text{GPa}\}$ ([35] used in eq. 5 in [25]). Following [36], this leads to a shear modulus and a Poisson's ratio of $\{\mu = 23.9\,\text{GPa}, \nu = 0.432\}$ for an isotropic consideration. The isotropic consideration is used in the internal stress calculation resulting from the dislocation configuration (eq. 15 and 17 in [25]). The length of the Burgers vector is set to $b = 0.287\,\text{nm}$ [37], the material specific drag coefficient to $B = 10^{-4}\,\text{sPa}$ ([38] used in eq. 14 in [25]) and the backstress parameter to $D = \frac{3.29}{2\pi^2(1-\nu)}$ ([32] used in eq. 15 in [25]). The coefficients of the material interaction matrix used in the yield stress term are chosen to $\{a_{self} = 0.3, a_{hirth} = 0.083, a_{lomer} = 0.326, a_{gliss} = 0.661, a_{coll} = 0.578\}$ ([39] used in eq. 17 in [25]). The constants for the cross-slip probabil-

4

ity term is assumed as $\beta = 10^5$ [40], the activation volume is set to $V_{\text{act}} = 17.2 \, b^3$ [41] and the stress initializing stage-three hardening is chosen to $\tau_{\text{III}} = 0.01 \, \text{GPa}$ [42] (used in eq. 20 in [26]). The critical source stress of the homogenized dislocation source model depends solely on the current microstructure (eq. 10 in [29]) and the dislocation reaction coefficients are chosen to $\{c_{\text{gliss}} = 0.064, c_{\text{Lomer}} = 0.096, c_{\text{coll}} = 0.0032\}$ (used in eq. 13 in [27]). It should be noted that due to the lack of data for the dislocation reaction coefficients in the case of gold under torsion, the exact choice of constants is uncertain. The dislocation reaction coefficients for the glissile reaction was taken from the literature for single crystalline aluminum under tensile loading in [43, 26, 27], whereas the coefficients for the Lomer and collinear reaction were adjusted ($c_{\text{Lomer}} = 1.5 \, c_{\text{gliss}}, \, c_{\text{coll}} = 0.05 \, c_{\text{gliss}}$ which differ from [27]). The chosen dislocation reaction coefficients ensure a plausible evolution of the torque compared to the experimental results and of the total dislocation density compared to DDD simulations according to [11]. The external torsional load is applied displacement-controlled at a rate of $\dot{\varphi} = 1° \, {}^1\!/_{\mu s}$ leading to a surface shear of $\dot{\gamma}_R = \dot{\varphi}/4 \approx 4.36 * 10^3 \, {}^1\!/_s$ for the considered circular microwires with diameters of $24 \, \mu m$. The initial microstructure state is assumed to have a total dislocation density of approximately $2.4 \times 10^{12} \, \text{m}^{-2}$ equally distributed on all slip systems.

The implementation of the CDD formulation used was integrated into a two-scale numerical framework based on [25] using an own customized version of the parallel finite element software M++ [44, 45]. Thereby, a finite element approach using tetrahedrons and linear ansatz functions for the displacements to solve the external stress field is combined with an implicit Runge-Kutta discontinous Galerkin scheme with full upwind flux and constant ansatz functions for the dislocation densities to solve the evolution of the microstructure. Simplifying but found to be efficient, the same mesh resolution is applied to both scales. An implicit midpoint rule with a fixed time step is used as time discretization.

2.3. Experimental methods
Sample preparation

In the experimental part of this study, Au microwires with a diameter of $25 \, \mu m$ were used. Since a preparation route for producing single crystalline wires with a suitable length of several millimetres for sample mounting and mechanical testing is not available, experiments were carried out using microwires with a so called bamboo structure. A bamboo structure can be obtained during annealing after full recrystallization of the polycrystalline microstructure. In case of a laterally structured thin film or a polycrystalline wire, the final grains extend through the entire cross-section of the sample and the microstructure consists of a chain of individual grains with preferred crystal orientation. For a metallic wire, it is thus possible to study the torsion of differently oriented single crystalline pieces along the wire axis.

To achieve this structure, the as-prepared, polycrystalline Au microwires (Heraeus, Germany) were annealed for 168 h at 800°C in a high vacuum glass tube furnace. The bamboo structure of the annealed samples consisted of grains close to the

$\langle 1\,0\,0 \rangle$ and $\langle 1\,1\,1 \rangle$ crystal orientation with respect to the wire axis. The orientation spread was ±10° with respect to the perfect crystal orientation. Grains with $\langle 1\,1\,0 \rangle$ orientation in relation to the wire axis were not found.

For the torsion experiments, a custom-built torsion setup for testing of microwires with diameters of 10–200 μm was used [46]. The torsion setup is mounted within a tensile testing device to allow a prestraining of the samples. The torsion setup is configured to twist a sample to a defined degree of deformation, given by the plastic shear at the outer radius $\gamma_{R,pl}$. As reference, $\gamma_{R,pl}$ is estimated for the plastic deformation to the whole sample. Effectively, the deformation in the individual grains is different and depends on the specific orientation of the individual grain. The deformation of the individual grain cannot be controlled and has to be measured locally.

Sample analysis

After the torsion experiment has been performed to the defined global plastic strain $\gamma_{R,pl}$, the wires were cut in several sections. The individual sections which were glued on sample stubs for further preparation in a Dual Beam focused ion beam scanning electron microscope (FIB-SEM) (FEI Nova NanoLab 200). The wire sections were scanned for specifically homogeneous grains having a preferred length of at least $30 \, \mu m$ and the desired crystal orientation close to $\langle 1\,0\,0 \rangle$ or $\langle 1\,1\,1 \rangle$. Selected grains were cut using the FIB to create planar cross-sections of the grain. The cross-sections of the samples were further analyzed using the integrated electron backscatter diffraction (EBSD) system (Oxford Instruments) of the microscope. The Kikuchi patterns were analyzed using the Cross Court 3 package for high resolution EBSD (HREBSD) [47, 48].

The data of the HREBSD analysis were analyzed by an inhouse-developed Matlab code [49]. To study the misorientation gradients along the cross-sections, the data were evaluated in two different ways, giving the global and local changes of crystal orientation [50]. Global changes of crystal orientation give hints about the rotation of the whole grains. Therefore, the misorientation at every position was calculated with respect to the center of the wire cross-section and was described using the axis-angle notation. In the axis-angle notation, the scalar value of misorientation is mapped, overlayed by arrows showing the axis of rotation, related to the orientation of the reference. The local misorientation, giving hints on the local dislocation structures and respective density of GNDs, was determined by calculating the misorientation between individual neighbouring data points. The individual neighbouring data points were specifically chosen with respect to the orientation of the intersection of a glide plane with the cross-section under investigation.

3. Results of the Microstructure Evolution

We study the microstructure evolution of single crystalline gold microwires under linearly increasing torsional loading for the three different high-symmetry crystal orientations $\langle 1\,0\,0 \rangle$, $\langle 1\,1\,0 \rangle$, and $\langle 1\,1\,1 \rangle$ as shown in Figure 1. The theoretical considerations according to subsection 2.1 are combined with simula-
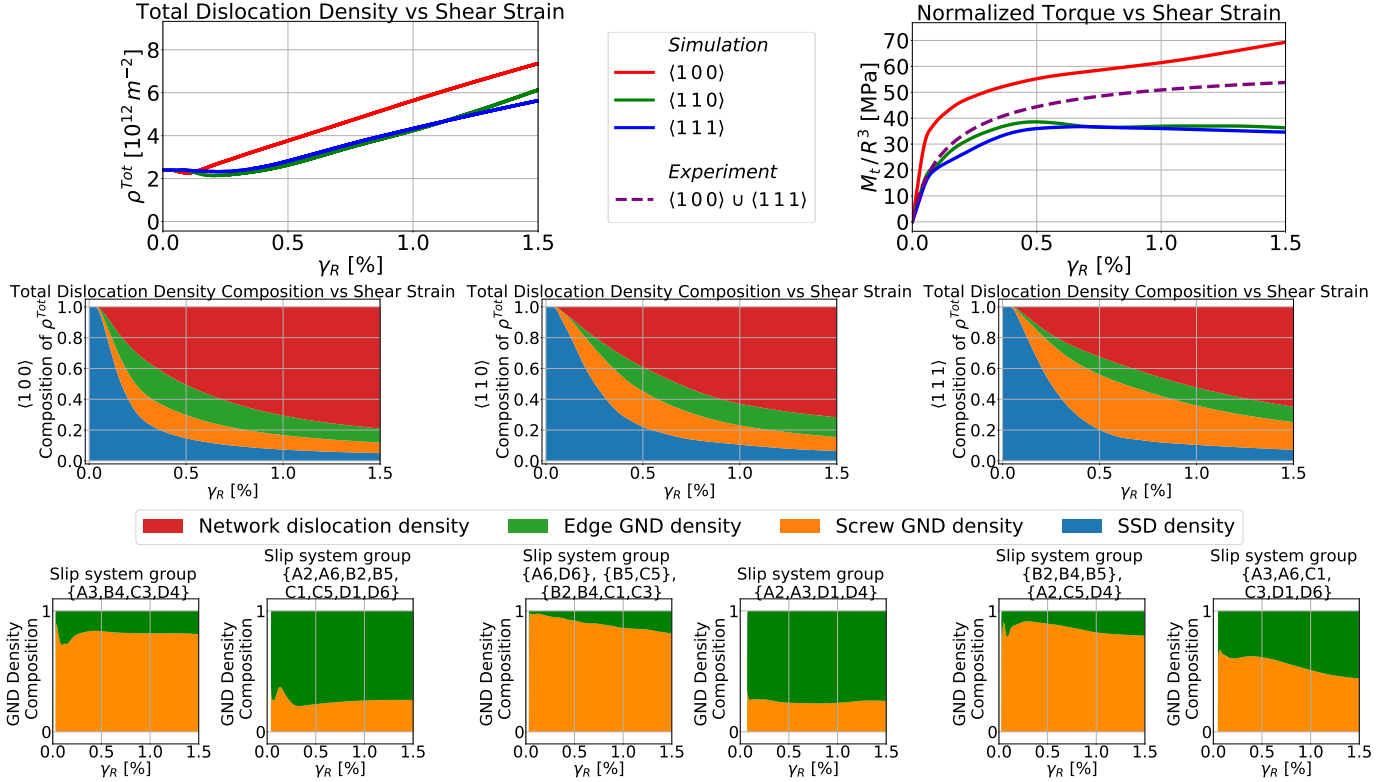
Figure 3: Evolution of the total dislocation densities and normalized torques over the surface shear strain including results from the simulation (single crystals) and experiment (entire bamboo structured wire). Furthermore, the composition of both the total dislocation densities and the GND densities are shown for the different crystal orientations: $\langle 1\,0\,0 \rangle$ on the left, $\langle 1\,1\,0 \rangle$ in the middle, and $\langle 1\,1\,1 \rangle$ on the right.

tion results, providing direct insight into the microstructure evolution. In comparison with experimental results, this provides insights into the classification and activity of the slip systems, the evolution and composition of the dislocation densities, as well as the effects on the misorientation in the microwire.

As shown in Figure 3, the total dislocation density in the simulation increases almost linearly with increasing strain after a certain initial (elastic) transition region for all three crystal orientations. Here, the density increase for the $\langle 1\,0\,0 \rangle$ orientation starts slightly earlier compared to the other orientations. The single crystalline gold exhibits a shear modulus value of $\mu_{\langle 1\,0\,0 \rangle} \approx 42\,\text{GPa}$ in the $\langle 1\,0\,0 \rangle$ orientation, which is more than twice as large compared to $\mu_{\langle 1\,1\,1 \rangle} \approx 19\,\text{GPa}$ in $\langle 1\,1\,1 \rangle$ and correlates with the higher gradient of the torsion curve in the elastic regime. Furthermore, the $\langle 1\,0\,0 \rangle$ orientation shows the highest material hardening compared to the other orientations. The experimentally determined torsion curve for the torsion wire with a bamboo structure of alternating $\langle 1\,0\,0 \rangle$ and $\langle 1\,1\,1 \rangle$ grains is located between the torsion curves for the single crystals in the simulation. It should be noted that due to the experimental setup, measurement data of the normalized torsion curve are only available starting from a value greater than $\sim 20\,\text{MPa}$ and has been extrapolated for lower stresses.

The simulation results provide insights into different types of dislocation densities and reveal that a significant amount of dis-

locations form a dislocation network. The GND density accumulates in the system, whereas the SSD fraction is decreasing during the evolution. However, it is remarked that the CDD formulation only resolves the GND character for the mobile dislocation density, not for the immobile dislocation network density. For a considered load of $\gamma_R = 1.5\,\%$, the total dislocation density consists of about $80\,\%$ of dislocation network density for the $\langle 1\,0\,0 \rangle$ orientation. Furthermore, the mobile GND dislocation density in all orientations consist of both screw and edge types, whereby the $\langle 1\,1\,1 \rangle$ orientation shows the highest screw proportion. A detailed examination reveals differences in the composition of the GND density in all orientations depending on the respective slip system groups. In the $\langle 1\,0\,0 \rangle$ orientation, e.g., the GND density in the slip system group {A3,B4,C3,D4} mainly shows a screw character, whereas in the slip system group {A2,A6,B2,B5,C1,C5,D1,D6} the edge character predominates.

The microstructure evolution leads to misorientations. This is characterized by the local misorientation angles and rotation axes in the respective microwire cross-sections with respect to the cross-section center as reference, see Figure 4. For all considered crystal orientations, larger misorientation angles are observed near the surface compared to region close to the center. The rotation axes for the $\langle 1\,0\,0 \rangle$ and $\langle 1\,1\,1 \rangle$ orientations point towards the cross-section center, whereas for the $\langle 1\,1\,0 \rangle$ orien-
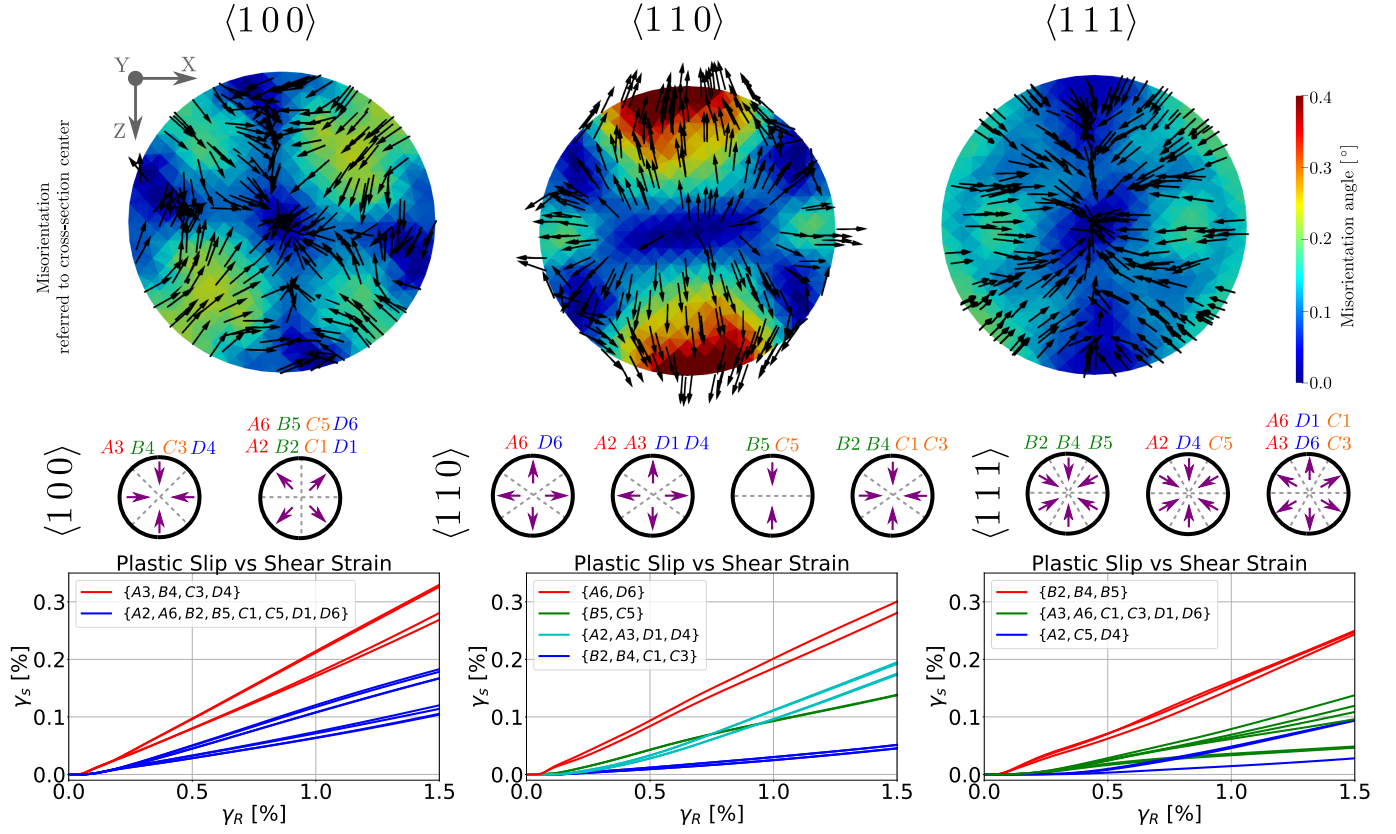
Figure 4: Map of the misorientation, characterized by the local misorientation angles and rotation axes in the respective microwire cross-sections with respect to the cross-section center as reference for the considered crystal orientations $\langle 1\,0\,0 \rangle$ (left), $\langle 1\,1\,0 \rangle$ (middle), and $\langle 1\,1\,1 \rangle$ (right). The maps refer to a total surface shear of $\gamma_R \approx 1.5\,\%$ corresponding to a plastic surface shear of $\gamma_{R,pl} \approx 0.7\,\%$. For comparison, the rotation axes of different slip system groups derived from the theoretical considerations are given below with respect to the crystal orientation. Furthermore, the evolution of the plastic slip averaged over the system is shown for the different slip system groups.
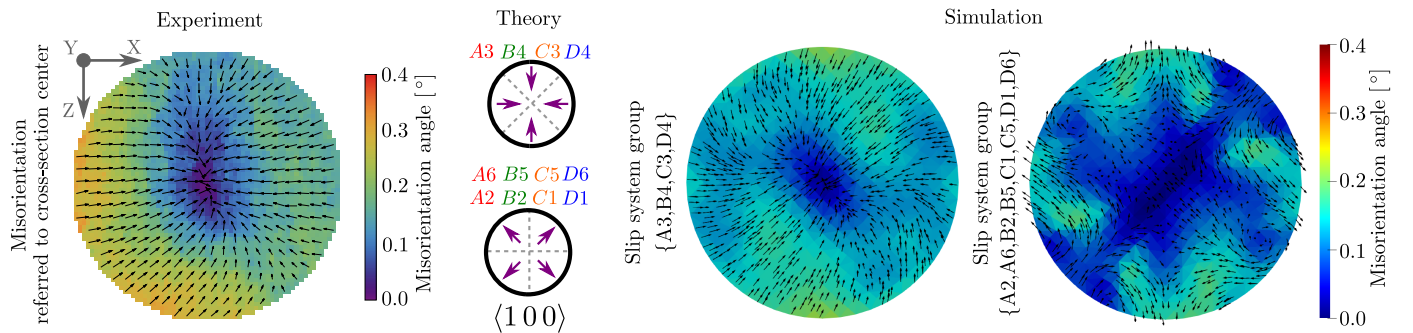
Figure 5: Comparison of experimental, theoretical, and simulation results for a $\langle 1\,0\,0 \rangle$ oriented microwire. Experimental HR-EBSD measurements for a plastic surface shear of $\gamma_{R,pl} \approx 0.8\,\%$ (left), theoretical rotation axes (middle) and simulation results for a total surface shear of $\gamma_R \approx 1.5\,\%$ corresponding to a plastic surface shear of $\gamma_{R,pl} \approx 0.7\,\%$ (right) are shown. For the simulation results, the misorientation resulting from the plastic slip on the respective slip system groups is visualized separately.

tation they point towards the surface. For comparison, Figure 4 also shows the orientations of the rotation axes for different slip system groups derived from the theoretical considerations in subsection 2.1. In addition, the plastic shear on the individual slip systems averaged over the system is shown. For the $\langle 1\,0\,0 \rangle$ orientations, the slip system group {B4,C3,A3,D4} shows the highest activity, whereas for $\langle 1\,1\,0 \rangle$ {A6,D6} and for $\langle 1\,1\,1 \rangle$ {B2,B4,B5} are primary active. In the $\langle 1\,1\,0 \rangle$ orientation, the slip system group {A2,A3,D1,D4} reaches a plastic shear up to 1.4 times higher compared to the slip system group {B5,B6}. For comparison with the slip system group {B2,B4,C1,C3}, it occurs up to 4 times higher, although the Schmid factors have an opposite tendency ($m_{A2} = m_{B2} = 0.5 < m_{B5} = 0.8$).

In the following, the system analysis and simulation will be used to gain insights into the experimental observations, exemplary shown for the $\langle 1\,0\,0 \rangle$ orientation in Figure 5. Figure 5 (left) shows the misorientation with respect to the cross-sectional center measured in the experiment. It can be observed that the rotation axes point to the wire center, with larger misorientation angles near the surface compared to regions close to the center. For comparison, the theoretical rotation axes as well as the simulation results are shown. In the latter, the misorientation resulting from plastic slip on the individual slip systems was calculated separately for the two slip system groups. The roation axes of the misorientation due to the plastic slip on the slip system group {B4,C3,A3,D4} points towards the center, whereas for the slip system group

{B2,B5,C1,C5,A2,A6,D1,D6} the rotation axes mainly point towards the surface in regions with higher misorientation angles.

The local misorientation with reference to the respective neighbor in [101] and [$\bar{1}$01] direction is shown in Figure 6. The experimental HR-EBSD measurements show bands with high local misorientation angles within the microwire cross-section. These bands are oriented orthogonal to the evaluation direction and therefore in $e_\phi(\phi = \pm 45°)$ direction. The local misorientation is less pronounced in the near-surface regions, which are located in the direction of the evaluation direction (upper left and bottom right or upper right and bottom left). For comparison, the theoretical stress-free lines of the individual slip systems as well as the spatial distribution of the simulated GND density and the dislocation network density of the slip systems {B4,D4} and {C3,A3} are shown as well in Figure 6. The stress-free lines of the slip system group {B4,C3,A3,D4} as well as the piled-up GND density and the dislocation network densities show the same orientation as the respective local misorientation in the experiment. A tendency of increase in the dislocation network density is observed from the respective stress-free line in orthogonal direction to the corresponding Burgers vector towards the surface. In contrast, the dislocation network densities in the near-surface regions located farthest away from the respective stress-free line are less pronounced.
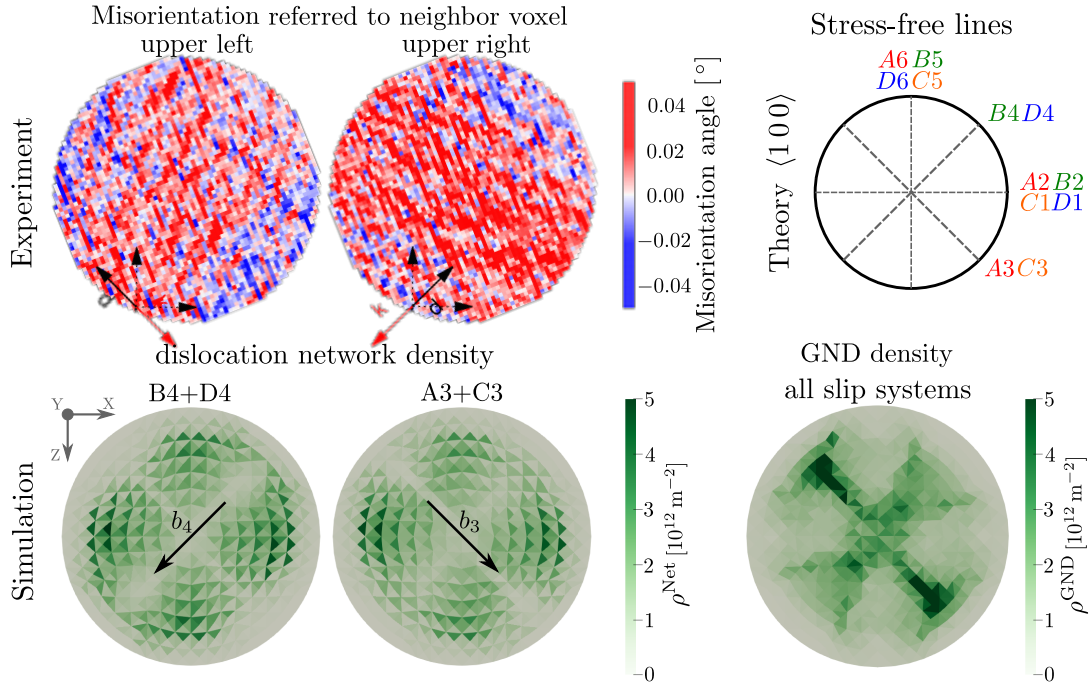
Figure 6: Comparison of experimental HR-EBSD measurements for a plastic surface shear of $\gamma_{R,pl} \approx 0.8\,\%$ (top left), theoretical considerations (top right) and simulation results for a total surface shear of $\gamma_R \approx 1.5\,\%$ corresponding to a plastic surface shear of $\gamma_{R,pl} \approx 0.7\,\%$ (bottom) for $\langle 1\,0\,0 \rangle$ oriented microwires. The misorientation with respect to the upper left and upper right neighbor voxel (in [101] and [$\bar{1}$01] direction) in the experiment is shown. For the simulation, the spatial distribution of the GND density and the dislocation network density of specific slip systems is depicted.

4. Discussion

The a priori theoretically derived classification of the slip systems into slip system groups based on the respective Schmid factors and dislocation reactions, see Table 2, could be confirmed by the CDD simulation results. The slip system group with the highest Schmid factor, see Table 1, is primarily active, see Figure 4. The primary activity of the slip systems with the highest Schmid factors as well as the contribution of other slip systems with lower Schmid factors are consistent with the DDD results of $\langle 1\,0\,0 \rangle$ and $\langle 1\,1\,1 \rangle$ oriented single crystalline aluminium microwires under torsion [11]. We compare our CDD results here to DDD simulations wherever possible since our CDD framework lacks the resolution of individual dislocations.

In the $\langle 1\,1\,0 \rangle$ orientation, we observe a higher plastic shear on the slip system group {A2,A3,D1,D4} compared to the slip system group {B2,B4,C1,C3}. Sharing the same Schmid factor, this can be explained by the dislocation reaction relationships. Considering dislocation reactions, glissile reactions initiated by the primary slip system group {A6,D6} lead to new mobile dislocations only in the slip system group {A2,A3,D1,D4}. In addition, geometric differences in the cross-sections of the slip planes have to be considered (the average cross-section area of slip plane {A,D} is about 1.6 times the area of slip plane {B,C}, compare Figure 1). Consequently, the Schmid factor alone is not necessarily informative about the activity of the slip system.

The torsion curves resulting from the simulation can be considered consistent with the experimental measurements as the experimental torsion curve for the entire microwire with a bamboo structure of alternating $\langle 1\,0\,0 \rangle$ and $\langle 1\,1\,1 \rangle$ grains is located between the torsion curves for the simulated single crystals, see Figure 3. Consequently, the bamboo structured microwire in the experiment can be interpreted as a serial connection of $\langle 1\,0\,0 \rangle$ and $\langle 1\,1\,1 \rangle$ grains. Of course, dislocation interactions with respect to the grain boundary in the bamboo structured microwire are neglected here.

Due to the inhomogeneous stress field of the torsion loading, an accumulation of GND density occurs and internal dislocation pile-ups form in the microwires. Thereby, the screw and edge type composition of the GND density depends on the slip system group and correlates with the theoretical considerations for fictitious GNDs parallel to the individual stress-free lines (cp. Figure 3 and Table 1). The primary slip system groups have a high proportion of screw character (e.g. the slip system group {B4,C3,A3,D4} in case of a $\langle 1\,0\,0 \rangle$ orientation), whereas other slip system groups have a higher proportion of edge character (e.g. the slip system group {B2,B5,C1,C5,A2,A6,D1,D6} in case of a $\langle 1\,0\,0 \rangle$ orientation). The exact composition of the overall GND density in the systems can be traced back to the ratio of the activities of the individual slip system groups. The composition of the GND density has a great influence on potentially occurring mechanisms in the microstructure, e.g., only screw dislocations can cross-slip. Cross-slip of dislocations evading the backstresses in the dislocation pile-ups can lead to redistribution of GNDs and thus plastic irreversibility, as observed

in [6, 51]. The spatial distribution of the GND density pile-up matches with the orientation of stress-free lines in the simulation as shown for the cross structure in case of a $\langle 1\,0\,0 \rangle$ orientation in Figure 6. This is consistent with the findings gained by DDD simulations of single crystalline microwires under torsion with $\langle 1\,0\,0 \rangle$, $\langle 1\,1\,0 \rangle$, and $\langle 1\,1\,1 \rangle$ orientations in [6, 7, 8], as well as MD simulations of single crystalline gold and aluminum nanowires under torsion with $\langle 1\,0\,0 \rangle$, $\langle 1\,1\,0 \rangle$, and $\langle 1\,1\,1 \rangle$ orientations in [5, 10].

During the microstructure evolution, a dislocation network forms as shown in Figure 3. This is also observed in DDD simulations of single crystalline aluminum microwires in [11] and copper nanowires in [13]. The increase in the total dislocation density for smaller loading in the $\langle 1\,0\,0 \rangle$ orientation compared to the other orientations studied (see Figure 3) is also observed in the DDD simulations in [7]. Reasons could be therefore: First, the anisotropy of the elastic properties (especially the shear modulus: $\frac{\mu_{\langle 1\,0\,0 \rangle}}{\mu_{\langle 1\,1\,1 \rangle}} \approx 2.2$ for gold), leads to higher stresses for the $\langle 1\,0\,0 \rangle$ orientation. Second, a higher number of slip systems in the primary slip system group for the $\langle 1\,0\,0 \rangle$ orientation is observed (cp. Table 2). Third, the comparatively smaller difference in Schmid factors between the primary and the other slip system groups (cp. Table 1) results in the earlier activation of the non-primary slip system groups compared to other orientations. It should be noted here, that in the DDD simulations in [11] for aluminum microwires modeled as elastically isotropic, an earlier increase in total dislocation density is observed for the $\langle 1\,1\,1 \rangle$ orientation compared to the $\langle 1\,0\,0 \rangle$ orientation, which can be attributed to the maximum Schmid factors (cp. Table 1: $\frac{m_{\langle 1\,0\,0 \rangle}^{\max}}{m_{\langle 1\,1\,1 \rangle}^{\max}} \approx 0.6$). The exact influence of the material, the system size, the dislocation reactions and initial dislocation structure remains to be clarified. However, in both [11] and this work, a nearly linear increase in the total dislocation densities is observed.

The combination of theoretical, experimental, and simulation results in this work provide fundamental insights into the system behavior and interaction principles of slip system activities. The various slip system groups differ with respect to their relaxation mechanism, which affects the misorientation as discussed in Figure 2. Accordingly, in the $\langle 1\,0\,0 \rangle$ and $\langle 1\,1\,1 \rangle$ orientation, stress relaxation is realized primarily by the transformation of the elastic deformation into plastic deformation, whereas in the $\langle 1\,1\,0 \rangle$ orientation an elastic counterpart is formed. It was shown that the direction of the rotation axes of the resulting misorientation can be used to draw conclusions about the primary slip system groups for the qualitatively known torsional load, see Figure 4. This approach can also be applied to experimental measurements, see Figure 5 with respect to the plastic slip given in Figure 4. Here, the slip system group {A3,B4,C3,D4} has been identified as the primary slip system group for a $\langle 1\,0\,0 \rangle$ oriented single crystal subjected to torsional load based on experimental measurements. Further investigations on $\langle 1\,1\,1 \rangle$ orientation indicate that the approach is applicable here as well since the experimental determined rotation axes of the misorientation point to the center of the cross-section. According to the system analysis, the orienta-

tion of rotation axes indicate that the slip system group with the highest Schmid factor {B2,B4,B5} is primary active.

The evaluation of the direction of the rotational axes of the misorientation can be used to obtain further information about the microstructure evolution including the activity of the slip system groups. Thereby, the analysis can be applied directly to the experimental measurements of the misorientation without the need for further steps and considers all twelve slip system of the fcc crystal structure in a 3d system. Limitations are that the load must be known for the evaluation and that only relative and no absolute activities can be derived. In addition, it is not possible to distinguish between slip system groups with the same relaxation principle. The evaluation approach complements other analysis methods, e.g. the analysis of the orientations of surface steps on SEM images or the analysis of the dominant Burgers vector based on the dislocation density tensor (α tensor [52, 53, 54]). The analysis of the orientations of surface steps provides information about active slip planes without revealing the respective slip systems involved. In contrast, the analysis of the dominant Burgers vector provides information about the dominant Burgers vector without revealing the associated slip plane or slip system [34]. It should be noted that in the dominant Burgers vector analysis, a superposition of Burgers vectors to another Burgers vector might occur, which might lead to ambiguous results. The identification of the GND densities on the individual slip systems starting from a determined dislocation density tensor is ambiguous due to the underconstrained nature of the equation system. The restriction of experimental measurements to individual surfaces leads to a reduction of the known α tensor components and consequently to an amplification of the problem. Consequently, further assumptions and calculation steps are necessary to solve the equation system, e.g. restricting to a smaller number of (representative) slip systems in a plane deformation state [21] or neglecting the elastic strain tensor and solving a minimization problem [22].

The experimentally ex situ observed structures in the local misorientation referring to the neighbor voxel for the ⟨1 0 0⟩ orientation, see Figure 5, can be interpreted as low angle twist boundaries or comparable dislocation structures. Here, the orientations of the formed structures in the local misorientation are aligned to dislocation network densities of the primary slip system group and GND density or theoretically derived stress-free lines of the primary active slip system group respectively. Therefore the results suggests an elemental role of dislocations on the primary slip system group {B4,C3,A3,D4}, which have mainly screw character, in the formation of twist boundaries for the ⟨1 0 0⟩ orientation. This is consistent with the results in [5, 13, 11]. The formation of a dislocation network has a stabilizing effect on the dislocation configuration and hinders the dislocations from leaving the system during unloading the system. The observed pronounced misorientation referring to the neighbor voxel in the majority of the cross-section of the microwire is thereby consistent with the tendency of an increasing dislocation network density from the respective stress-free line in orthogonal direction to the corresponding Burgers vector towards the surface. The tendency of less pronounced local misorientations referring to the neighbor voxel and of the dis-

location network densities in the near-surface regions located farthest away from the respective stress-free lines might be attributed to the higher local resolved shear stresses there. The higher resolved shear stresses on the slip systems could lead to a dissolution of the formed dislocation junctions or even prevent their formation.

In addition to the globally resulting torsion curve, the approach used in this work enables to compare the spatial distribution of local activities of slip system groups between simulation and experiment. This provides meaningful insights into the microstructure evolution that are not easy to access by solely experimental investigations. However, although the simulation shows reasonable microstructure evolution results consistent to the experimental torsion curves, also differences can be observed. In the simulation, for the ⟨1 0 0⟩ orientation four symmetrically arranged areas with low misorientations near the surface are observed, see Figure 4. This spatial distribution can be attributed to the superposition of the activities of the slip system group {A3,B4,C3,D4} and {B2,B5,C1,C5,A2,A6,D1,D6}, compare Figure 5. Such spatial characteristic is not observed in the experiment, see Figure 5. Consequently, this indicates that the higher activity of the primary slip system group {A3,B4,C3,D4} is even more pronounced in the experiment than it is the case in the simulation. The underestimation of the activity of the primary slip system group in the simulation can have various origins and motivates a more detailed investigation of the chosen values for the reaction constants and cross-slip parameters as well as of the initial microstructure. A detailed investigation of the initial dislocation configurations in the experiment as well as an analysis of the reaction parameters based on a comprehensive DDD data set including different loading types, crystal orientations, and materials would be informative, but is beyond the scope of this work.

It should be noted that although the misorientation measured ex situ in the experiment is based on the distortion of the crystal lattice due to currently existing dislocations, whereas the misorientation in the simulation is based on the plastic deformation that has taken place, a correlation of the two quantities is assumed here. First, the DDD studies in [13] indicate a stable dislocation network and rather low plastic recovery in the unloading process for the ⟨1 0 0⟩ orientation, Therefore the differences between in situ and ex situ measurements of the misorientation are assumed to be negligible in this case. Furthermore, due to the dislocation pile-up resulting from the inhomogeneous stress field, the GND density depend on the slip system activities. Thus, the GND density can be used to estimate the slip system activity. This may no longer be the case for a homogeneous load, since the GND density may be primarily located on the rather passive slip systems, see e.g. [55, 34].

Finally, it should be remarked that due to possible geometric imperfections and heterogeneous microstructures, localizations of plastic deformations may occur in the microwires, which are not represented by the continuum formulation. Nevertheless, the findings gained in this work on the interaction principles of the slip system activities and relaxation mechanisms are general and show reasonable results.

5. Conclusion

In this paper the microstructure evolution of single crystalline gold microwires under torsional loading has been studied for the high-symmetry crystal orientations $\langle 1\,0\,0 \rangle$, $\langle 1\,1\,0 \rangle$, and $\langle 1\,1\,1 \rangle$ using theoretical, simulation and experimental results. It has been shown that a classification of the slip systems into slip system groups based on the respective Schmid factors and dislocation reaction relationships can be derived a priori by theoretical considerations and that the slip system activity, stress relaxation mechanism, as well as screw and edge composition of the piled-up GND density is depending on the respective slip system group. Furthermore, it has been shown that conclusions can be drawn about the active slip system groups based on the direction of the rotational axes of the misorientations. This method of analysis is also applicable to experimental results. For the $\langle 1\,0\,0 \rangle$ orientation, it was found that the primary slip system group is essentially responsible for the formation of low angle twist boundaries.

Declaration of Competing Interest

The authors declare that they have no known competing financial interests or personal relationships that could have appeared to influence the work reported in this paper.

Acknowledgement

Appendix A. Misorientation from distortion fields

The skew symmetric part of the plastic distortion tensor can be interpreted as an infinitesimal rotation tensor $\mathbf{W}$. The infinitesimal rotation tensor is characterized by an angle α around a normalized rotation axis $\mathbf{n}^{\mathrm{rot}} = (n_x^{\mathrm{rot}}\, n_y^{\mathrm{rot}}\, n_z^{\mathrm{rot}})^T$ describing the remaining rotation from the initial configuration into the actual one:

$$\mathbf{W} = \mathrm{skw}(\boldsymbol{\beta}^{\mathrm{pl}}) = \alpha \begin{pmatrix} 0 & -n_z^{\mathrm{rot}} & n_y^{\mathrm{rot}} \\ n_z^{\mathrm{rot}} & 0 & -n_x^{\mathrm{rot}} \\ -n_y^{\mathrm{rot}} & n_x^{\mathrm{rot}} & 0 \end{pmatrix}, \quad \alpha = \|\alpha \mathbf{n}^{\mathrm{rot}}\|.$$

(A.1)

The rotation matrix results in

$$\mathbf{R} = \cos(\alpha)\mathbb{1} + (1 - \cos(\alpha))(\mathbf{n}^{\mathrm{rot}} \otimes \mathbf{n}^{\mathrm{rot}}) + \sin(\alpha)\frac{1}{\alpha}\mathbf{W}^T. \quad \text{(A.2)}$$

The misorientation characterizes the misalignment of the considered configuration compared to a reference configuration. Thus, the misorientation is based on the rotation matrix $\mathbf{R}$ at each site and the rotation matrix $\mathbf{R}^{\mathrm{ref}}$ of the reference continuum in order to identify the misorientation angle θ:

$$\theta = \arccos\left(\frac{\mathrm{trace}(\mathbf{R}^{\mathrm{mis}}) - 1}{2}\right) \quad , \quad \mathbf{R}^{\mathrm{mis}} = \mathbf{R}^{\mathrm{ref}}\mathbf{R}^{-1} \quad \text{(A.3)}$$

$$\mathbf{n}^{\mathrm{mis}} = \frac{1}{2\sin(\theta)}\begin{pmatrix} R_{yz}^{\mathrm{mis}} - R_{zy}^{\mathrm{mis}} \\ R_{zx}^{\mathrm{mis}} - R_{xz}^{\mathrm{mis}} \\ R_{xy}^{\mathrm{mis}} - R_{yx}^{\mathrm{mis}} \end{pmatrix}. \quad \text{(A.4)}$$

If the reference is identical to the initial configuration, the following relations are valid: $\mathbf{R}^{\mathrm{ref}} = \mathbb{1}$, $\theta = \alpha$ and $\mathbf{n}^{\mathrm{mis}} = \mathbf{n}^{\mathrm{rot}}$.

References

[1] E. Schmid, W. Boas, Kristallplastizität : mit besonderer Berücksichtigung der Metalle, Struktur und Eigenschaften der Materie in Einzeldarstellungen ; 17, Springer, Berlin, 1935. doi:10.1007/978-3-662-34532-0.

[2] N. Fleck, G. Muller, M. Ashby, J. Hutchinson, Strain gradient plasticity: theory and experiment, Acta Metallurgica et materialia 42 (2) (1994) 475–487. doi:10.1016/0956-7151(94)90502-9.

[3] T. Zhu, A. Bushby, D. Dunstan, Materials mechanical size effects: a review, Materials Technology 23 (4) (2008) 193–209. doi:10.1179/175355508X376843.

[4] Y. Chen, O. Kraft, M. Walter, Size effects in thin coarse-grained gold microwires under tensile and torsional loading, Acta Materialia 87 (2015) 78–85. doi:10.1016/j.actamat.2014.12.034.

[5] C. R. Weinberger, W. Cai, Orientation-dependent plasticity in metal nanowires under torsion: Twist boundary formation and eshelby twist, Nano letters 10 (1) (2009) 139–142. doi:10.1021/nl903041m.

[6] J. Senger, D. Weygand, O. Kraft, P. Gumbsch, Dislocation microstructure evolution in cyclically twisted microsamples: a discrete dislocation dynamics simulation, Modelling and Simulation in Materials Science and Engineering 19 (7) (2011) 074004. doi:10.1088/0965-0393/19/7/074004.

[7] R. Jones, J. Zimmerman, G. Po, Comparison of dislocation density tensor fields derived from discrete dislocation dynamics and crystal plasticity simulations of torsion, Journal of Materials Science Research 5 (4) (2016) 44–62. doi:10.5539/jmsr.v5n4p44.

[8] I. Ryu, W. Cai, W. D. Nix, H. Gao, Anisotropic size-dependent plasticity in face-centered cubic micropillars under torsion, JOM 68 (1) (2016) 253–260. doi:10.1007/s11837-015-1692-1.

[9] S. Quilici, S. Forest, G. Cailletaud, On sire effects in torsion of multi-and polycrystalline specimens, Le Journal de Physique IV 8 (PR8) (1998) Pr8–325. doi:10.1051/jp4:1998840.

[10] C. R. Weinberger, W. Cai, Plasticity of metal wires in torsion: Molecular dynamics and dislocation dynamics simulations, Journal of the Mechanics and Physics of Solids 58 (7) (2010) 1011–1025. doi:10.1016/j.jmps.2010.04.010.

[11] M. Stricker, M. Ziemann, M. Walter, S. M. Weygand, P. A. Gruber, D. Weygand, Dislocation structure analysis in the strain gradient of torsion loading: a comparison between modelling and experiment, Modelling and Simulation in Materials Science and Engineering 30 (3) (2022) 035007. doi:10.1088/1361-651x/ac4d77.

[12] L. Bardella, A. Panteghini, Modelling the torsion of thin metal wires by distortion gradient plasticity, Journal of the Mechanics and Physics of Solids 78 (2015) 467–492. doi:10.1016/j.jmps.2015.03.003.

[13] J. Gravell, S. Lee, S. Ryu, I. Ryu, Effect of size and orientation on stability of dislocation networks upon torsion loading and unloading in fcc metallic micropillars, Acta Materialia 214 (2021) 117010. doi:10.1016/j.actamat.2021.117010.

[14] M. Kaluza, K. Le, On torsion of a single crystal rod, International Journal of Plasticity 27 (3) (2011) 460–469. doi:10.1016/j.ijplas.2010.07.003.

[15] K. C. Le, Y. Piao, Distribution of dislocations in twisted bars, International Journal of Plasticity 83 (2016) 110–125. doi:10.1016/j.ijplas.2016.04.006.

[16] D. Liu, Y. He, D. J. Dunstan, B. Zhang, Z. Gan, P. Hu, H. Ding, Toward a further understanding of size effects in the torsion of thin metal wires: an experimental and theoretical assessment, International Journal of Plasticity 41 (2013) 30–52. `doi:10.1016/j.ijplas.2012.08.007`.

[17] D. Liu, X. Zhang, Y. Li, D. Dunstan, Critical thickness phenomenon in single-crystalline wires under torsion, Acta Materialia 150 (2018) 213–223. `doi:10.1016/j.actamat.2018.03.022`.

[18] K. C. Le, Y. Piao, Thermodynamic dislocation theory: Size effect in torsion, International Journal of Plasticity 115 (2019) 56–70. `doi:10.1016/j.ijplas.2018.11.009`.

[19] E. Bayerschen, A. Prahs, S. Wulfinghoff, M. Ziemann, P. Gruber, M. Walter, T. Böhlke, Modeling contrary size effects of tensile-and torsion-loaded oligocrystalline gold microwires, Journal of materials science 51 (16) (2016) 7451–7470. `doi:10.1007/s10853-016-0020-7`.

[20] M. Ziemann, Y. Chen, O. Kraft, E. Bayerschen, S. Wulfinghoff, C. Kirchlechner, N. Tamura, T. Böhlke, M. Walter, P. Gruber, Deformation patterns in cross-sections of twisted bamboo-structured au microwires, Acta Materialia 97 (2015) 216–222. `doi:10.1016/j.actamat.2015.06.012`.

[21] J. W. Kysar, Y. X. Gan, T. L. Morse, X. Chen, M. E. Jones, High strain gradient plasticity associated with wedge indentation into face-centered cubic single crystals: geometrically necessary dislocation densities, Journal of the Mechanics and Physics of Solids 55 (7) (2007) 1554–1573. `doi:10.1016/j.jmps.2006.09.009`.

[22] T. Ruggles, D. Fullwood, J. Kysar, Resolving geometrically necessary dislocation density onto individual dislocation types using ebsd-based continuum dislocation microscopy, International Journal of Plasticity 76 (2016) 231–243. `doi:10.1016/j.ijplas.2015.08.005`.

[23] T. Hochrainer, M. Zaiser, P. Gumbsch, A three-dimensional continuum theory of dislocation systems: kinematics and mean-field formulation, Philosophical Magazine 87 (8-9) (2007) 1261–1282. `doi:10.1080/14786430600930218`.

[24] T. Hochrainer, S. Sandfeld, M. Zaiser, P. Gumbsch, Continuum dislocation dynamics: towards a physical theory of crystal plasticity, Journal of the Mechanics and Physics of Solids 63 (2014) 167–178. `doi:10.1016/j.jmps.2013.09.012`.

[25] K. Schulz, L. Wagner, C. Wieners, A mesoscale continuum approach of dislocation dynamics and the approximation by a runge-kutta discontinuous galerkin method, International Journal of Plasticity 120 (2019) 248–261. `doi:10.1016/j.ijplas.2019.05.003`.

[26] M. Sudmanns, M. Stricker, D. Weygand, T. Hochrainer, K. Schulz, Dislocation multiplication by cross-slip and glissile reaction in a dislocation based continuum formulation of crystal plasticity, Journal of the Mechanics and Physics of Solids 132 (2019) 103695. `doi:10.1016/j.jmps.2019.103695`.

[27] M. Sudmanns, J. Bach, D. Weygand, K. Schulz, Data-driven exploration and continuum modeling of dislocation networks, Modelling and Simulation in Materials Science and Engineering 28 (6) (2020) 065001. `doi:10.1088/1361-651x/ab97ef`.

[28] T. Hochrainer, Multipole expansion of continuum dislocations dynamics in terms of alignment tensors, Philosophical Magazine 95 (12) (2015) 1321–1367. `doi:10.1080/14786435.2015.1026297`.

[29] K. Zoller, K. Schulz, Analysis of single crystalline microwires under torsion using a dislocation-based continuum formulation, Acta Materialia 191 (2020) 198–210. `doi:10.1016/j.actamat.2020.03.057`.

[30] K. Schulz, D. Dickel, S. Schmitt, S. Sandfeld, D. Weygand, P. Gumbsch, Analysis of dislocation pile-ups using a dislocation-based continuum theory, Modelling and Simulation in Materials Science and Engineering 22 (2) (2014) 025008. `doi:10.1088/0965-0393/22/2/025008`.

[31] I. Groma, F. Csikor, M. Zaiser, Spatial correlations and higher-order gradient terms in a continuum description of dislocation dynamics, Acta Materialia 51 (5) (2003) 1271–1281. `doi:10.1016/S1359-6454(02)00517-7`.

[32] S. Schmitt, P. Gumbsch, K. Schulz, Internal stresses in a homogenized representation of dislocation microstructures, Journal of the Mechanics and Physics of Solids 84 (2015) 528–544. `doi:10.1016/j.jmps.2015.08.012`.

[33] P. Franciosi, M. Berveiller, A. Zaoui, Latent hardening in copper and aluminium single crystals, Acta Metallurgica 28 (3) (1980) 273–283. `doi:10.1016/0001-6160(80)90162-5`.

[34] K. Zoller, S. Kalácska, P. D. Ispánovity, K. Schulz, Microstructure evolu-

tion of compressed micropillars investigated by in situ HR-EBSD analysis and dislocation density simulations, Comptes Rendus. PhysiqueOnline first (2021). `doi:10.5802/crphys.55`.

[35] J. Rösler, H. Harders, M. Bäker, Mechanisches Verhalten der Werkstoffe, Springer-Verlag, 2019. `doi:10.1007/978-3-658-26802-2`.

[36] E. Date, K. Andrews, Anisotropic and composition effects in the elastic properties of polycrystalline metals, Journal of Physics D: Applied Physics 2 (10) (1969) 1373. `doi:10.1088/0022-3727/2/10/303`.

[37] W. P. Davey, Precision measurements of the lattice constants of twelve common metals, Physical Review 25 (6) (1925) 753. `doi:10.1103/PhysRev.25.753`.

[38] J. Zhang, Y. Zhang, N. A. Mara, J. Lou, L. Nicola, Direct nanoimprinting of single crystalline gold: Experiments and dislocation dynamics simulations, Applied surface science 290 (2014) 301–307. `doi:10.1016/j.apsusc.2013.11.072`.

[39] S. Akhondzadeh, R. B. Sills, N. Bertin, W. Cai, Dislocation density-based plasticity model from massive discrete dislocation dynamics database, Journal of the Mechanics and Physics of Solids 145 (2020) 104152. `doi:10.1016/j.jmps.2020.104152`.

[40] D. Weygand, L. Friedman, E. Van der Giessen, A. Needleman, Aspects of boundary-value problem solutions with three-dimensional dislocation dynamics, Modelling and Simulation in Materials Science and Engineering 10 (4) (2002) 437. `doi:10.1088/0965-0393/10/4/306`.

[41] G. Saada, Cross-slip and work hardening of fcc crystals, Materials Science and Engineering: A 137 (1991) 177–183. `doi:10.1016/0921-5093(91)90333-I`.

[42] J. F. Bell, Generalized large deformation behaviour for face-centred cubic solids: Nickel, aluminium, gold, silver and lead, The Philosophical Magazine: A Journal of Theoretical Experimental and Applied Physics 11 (114) (1965) 1135–1156. `doi:10.1080/14786436508224924`.

[43] F. Roters, M. Diehl, P. Shanthraj, P. Eisenlohr, C. Reuber, S. L. Wong, T. Maiti, A. Ebrahimi, T. Hochrainer, H.-O. Fabritius, et al., Damask–the düsseldorf advanced material simulation kit for modeling multi-physics crystal plasticity, thermal, and damage phenomena from the single crystal up to the component scale, Computational Materials Science 158 (2019) 420–478. `doi:10.1016/j.commatsci.2018.04.030`.

[44] C. Wieners, Distributed point objects. a new concept for parallel finite elements, in: Domain decomposition methods in science and engineering, Springer, 2005, pp. 175–182. `doi:10.1007/3-540-26825-1_14`.

[45] C. Wieners, A geometric data structure for parallel finite elements and the application to multigrid methods with block smoothing, Computing and visualization in science 13 (4) (2010) 161–175. `doi:10.1007/s00791-010-0135-3`.

[46] M. Walter, O. Kraft, A new method to measure torsion moments on small-scaled specimens, Review of Scientific Instruments 82 (3) (2011) 035109. `doi:10.1063/1.3557824`.

[47] A. J. Wilkinson, G. Meaden, D. J. Dingley, High-resolution elastic strain measurement from electron backscatter diffraction patterns: new levels of sensitivity, Ultramicroscopy 106 (4-5) (2006) 307–313. `doi:10.1016/j.ultramic.2005.10.001`.

[48] A. J. Wilkinson, G. Meaden, D. J. Dingley, High resolution mapping of strains and rotations using electron backscatter diffraction, Materials Science and Technology 22 (11) (2006) 1271–1278. `doi:10.1179/174328406X130966`.

[49] M. Ziemann, Versetzungsstrukturen in tordierten goldmikrodrähten mit einer bambusstruktur, Ph.D. thesis, Karlsruher Institut für Technologie (KIT) (2020). `doi:10.5445/IR/1000122624`.

[50] L. N. Brewer, D. P. Field, C. C. Merriman, Mapping and Assessing Plastic Deformation Using EBSD, Springer US, Boston, MA, 2009, pp. 251–262. `doi:10.1007/978-0-387-88136-2_18`.

[51] C. Kirchlechner, P. J. Imrich, W. Liegl, J. Pörnbacher, J.-S. Micha, O. Ulrich, C. Motz, On the reversibility of dislocation slip during small scale low cycle fatigue, Acta Materialia 94 (2015) 69–77. `doi:10.1016/j.actamat.2015.04.020`.

[52] J. Nye, Some geometrical relations in dislocated crystals, Acta Metall. 1 (2) (1953) 153–162. `doi:10.1016/0001-6160(53)90054-6`.

[53] E. Kröner, G. Rieder, Kontinuumstheorie der versetzungen, Zeitschrift für Physik 145 (4) (1956) 424–429. `doi:10.1007/BF01338623`.

[54] B. A. Bilby, R. Bullough, E. Smith, Continuous distributions of dislocations: a new application of the methods of non-riemannian geometry, Proceedings of the Royal Society of London. Series A. Mathematical and

Physical Sciences 231 (1185) (1955) 263–273. `doi:10.1098/rspa.1955.0171`.

[55] C. Kirchlechner, D. Kiener, C. Motz, S. Labat, N. Vaxelaire, O. Perroud, J.-S. Micha, O. Ulrich, O. Thomas, G. Dehm, et al., Dislocation storage in single slip-oriented cu micro-tensile samples: new insights via x-ray microdiffraction, Philosophical Magazine 91 (7-9) (2011) 1256–1264. `doi:10.1080/14786431003785639`.